

Fast Micron-Scale 3D Printing with a Resonant-Scanning Two-Photon Microscope

Benjamin W. Pearre (1),
Christos Michas (2),
Jean-Marc Tsang (2),
Timothy J. Gardner (1,2),
Timothy M. Otchy (1)

((1) Dept of Biology, Boston University, Boston, MA, USA,
(2) Dept of Biomedical Engineering, Boston University, Boston, MA, USA)

Abstract

3D printing allows rapid fabrication of complex objects from digital designs. One 3D-printing process, direct laser writing, polymerises a light-sensitive material by steering a focused laser beam through the shape of the object to be created. The highest-resolution direct laser writing systems use a femtosecond laser to effect two-photon polymerisation. The focal (polymerisation) point is steered over the shape of the desired object with mechanised stages or galvanometer-controlled mirrors. Here we report a new high-resolution direct laser writing system that employs a resonant mirror scanner to achieve a significant increase in printing speed over galvanometer- or piezo-based methods while maintaining resolution on the order of a micron. This printer is based on a software modification to a commercially available resonant-scanning two-photon microscope. We demonstrate the complete process chain from hardware configuration and control software to the printing of objects of approximately $400 \times 400 \times 350 \mu\text{m}$, and validate performance with objective benchmarks. Released under an open-source license, this work makes micro-scale 3D printing available the large community of two-photon microscope users, and paves the way toward widespread availability of precision-printed devices.

Comments: Corresponding author: BWP (bwpearre@bu.edu). TJG and TMO contributed equally to this work.

Conflict-of-Interest statement: TJG is an employee of Neuralink Inc.

Keywords: 3d printing, additive manufacturing, lithography, direct laser writing, DLW, two-photon microscopy, resonant scanning.

1 Introduction

Direct laser writing (DLW) lithography [Maruo et al., 1997] is a 3D-printing technology that can be used to fabricate small-scale objects with complex geometries by programmatically exposing a light-sensitive material to a focused laser beam [Atwater et al., 2011, Buckmann et al., 2012, Cumpston et al., 1999, Farsari and Chichkov, 2009, Gissibl et al., 2016b]. Using femtosecond laser pulses and two-photon polymerisation processes to write a solid object structure into a photoresist, DLW enables on-demand fabrication of complex 3D objects with micron-scale features [Gissibl et al., 2016a, Malinauskas et al., 2010, 2013, Niesler and Tanguy, 2016, Farsari and Chichkov, 2009, Kabouraki et al., 2015, Gattass and Mazur, 2008, Sun and Kawata, 2004, Skylar-Scott et al., 2017, Gottmann, 2009]. While DLW achieves diffraction-limited resolution, the printing speed of DLW is slow, practically limiting the size of printed objects to millimetres. This speed limitation is changing rapidly, with a number of advancements reported. The slowest DLW printers use piezo stages, at speeds ranging from ~ 0.1 –30 millimetres per second [Straub and Gu, 2002, Ovsianikov et al., 2011]. Galvanometer-based printers can bring the laser scan rate up to tens or hundreds of mm/s [Thiel et al., 2010, Maruo and Ikuta, 2000, Farsari et al., 2006, Obata et al., 2013, Gottmann, 2009]. Recent reports include raster-scanned printing with high-speed galvanometers that achieve up to 400 mm/s [Skylar-Scott et al., 2016] by operating the scan mirror near its resonant frequency. Here we extend this trend by incorporating a resonant mirror operating at 8 kHz, which allows printing at speeds up to ~ 8000 mm/s.

In order to increase not only the speed of this technology but also its flexibility and availability, we present a raster-scanning DLW (rDLW) system built on a standard resonant-scanning two-photon microscope and open-source control software that are common equipment in many physical and life science laboratories. Open design and standard commercial components offer easy modification and adaptation to accommodate new materials, object sizes, and techniques.

We demonstrate the capabilities of our resonant rDLW printer in the fabrication of micron-scale objects. The instantiation reported here is capable of fabricating objects that are up to $\sim 400 \times 400 \times 350 \mu\text{m}$ with minimum feature sizes of $\sim 4 \times 1 \times 2 \mu\text{m}$ (X, Y, and Z, respectively), and with finer X-axis features available through the use of the microscope’s zoom. (We note that much larger objects may be constructed by stitching together overlapping pieces of this size, although a full discussion of this topic is beyond the scope of this work.) We show that the use of a resonant scanner allows our system to print an object of this size and arbitrary geometric complexity in about 20 seconds—a significant increase in printing speed over fast galvanometer-based systems. We evaluate performance with objective metrics assessed using IP-Dip (Nanoscribe, GmbH), a proprietary refraction-index-matched resist developed specifically for rapid, high-resolution DLW, although we expect that a wide variety of photoresists may be used.

Finally, we release our application software under an open-source license. Taken together, this work provides a new platform for innovation in DLW and

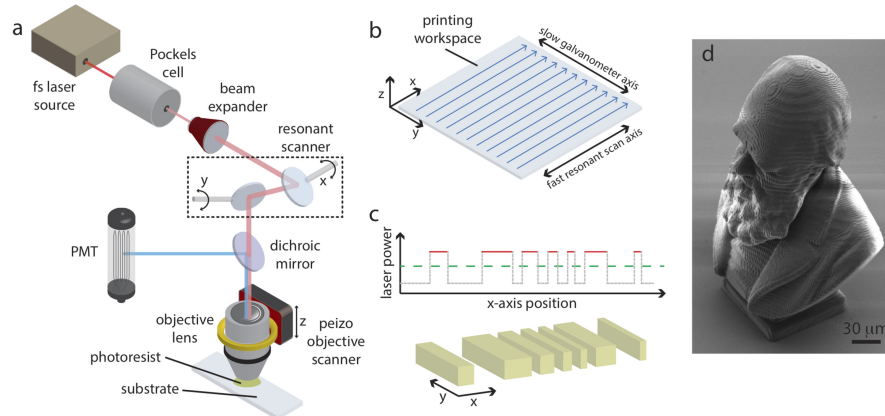


Figure 1: Overview of the resonant rDLW printer. (a) Schematic of the optical path from laser source to printed object. (b) The raster scanner rapidly sweeps the laser focus across the X axis of the printing workspace. (c) Top: laser power is modulated above (red line) and below (grey dotted line) the polymerisation threshold (green dashed line) throughout the X-axis sweep. Bottom: by applying this pattern of laser modulation across the workspace, solid features can be built up line by line and layer by layer. (d) SEM micrograph of a Charles Darwin statuette printed with our rDLW printer.

makes this technology more easily accessible to the community of two-photon microscope users.

2 Results

The rDLW system we report fabricates objects by raster-scanning the focal point of a femtosecond laser through a volume of photoresist, defining the object structure line by line. The device schematic in Fig. 1a depicts the hardware configuration tested and reported here—essentially, a standard two-photon microscope with a resonant raster scanner and high-speed/high-extinction-ratio laser power modulator. This schematic need not be taken as prescriptive, as one of the benefits to having an open system is the ability to modify components to meet the requirements of new applications.

2.1 A 3D printer built on a two-photon microscope

Our printer was built around a commercial two-photon microscope platform. A resonant+galvanometer scan module controls the laser’s X-Y focal point within the printable workspace. (Throughout the manuscript, we use Cartesian coordinates to refer to directions and dimensions in the printing workspace. Following

this nomenclature, X and Y are the perpendicular axes spanning a single focal plane of the orthogonal Z direction. In keeping with this, X denotes the direction of the high-speed (7.91 kHz) raster scanner’s sweeps, and Y identifies the slow galvanometer-controlled row index (Fig. 1b)). An immersion objective lens (25× magnification; numerical aperture (NA) of 0.8) with a refraction compensation ring was used for both printing and imaging. A piezo scanner enabled fast, precise Z-axis positioning of the objective lens (and hence the focal plane) during printing. A photomultiplier camera allowed imaging of the workspace and printed objects.

A tunable Ti-Sapphire laser system (~120 fs pulse duration, 80 MHz repetition) provided the light for both polymerisation and visualisation of the photoresist and printed objects. We used pump laser powers in the range of 6–10 W, resulting in a ~600–1000-mW mode-locked output beam at the polymerisation half-wavelength (tunable, but typically 780 nm). Beam intensity was modulated by a Pockels cell (ConOptics 350-80 cell and 302RM voltage amplifier) interfaced with a 3.33-MHz DAC (we note that this Pockels cell and driver are not rated for 3-MHz use, but the nonlinearity of the polymerisation reaction allows us to control printing voxelisation at a frequency higher than that for which the Pockels cell is rated. Nonetheless, we recommend that users work with a faster Pockels cell and driver in order to improve small-feature accuracy). Laser intensity was continuously monitored by sampling the passing beam. To flatten the profile and improve collimation, the beam was routed through a 2× Galilean beam expander before entering the microscopy optics (Fig. 1a).

All components were interfaced with the control computer via a dedicated data acquisition system. Vibration due to floor movements was minimised by building the rDLW system on an air-shock isolation table.

2.2 PrintImage: a resonant-rDLW control application

Because the printer is built on a two-photon microscope, we chose to use a popular open-source microscopy software package, ScanImage (Vidrio Technologies; Version \geq 5.2.3) [Pologruto et al., 2003], as the basis for system control. To implement printer functionality, we developed a custom MATLAB application, PrintImage, that runs alongside ScanImage to control print object voxelisation, calculate the laser power modulation sequence, and manage the printing-specific parts of the imaging process.

Print objects may be designed using any computer-aided-design or engineering (CAD/CAE) software capable of exporting Stereolithography (STL) files. STL files, which define the unstructured triangulated surface of the object by the unit normal and vertices of the triangles using a 3D Cartesian coordinate system, are transformed into a “watertight” solid object of specific dimensions that is mapped onto the predefined set of printer positions via a mesh voxelisation routine. Voxel Y and Z positions are determined by the number of scan lines and vertical slices specified by the user; X positions are computed as described below.

Once the object is voxelised, the series of filled and empty voxels along the

X direction of each Y row (blue arrows, Fig. 1b) is converted into a vector of supra- and sub-polymerisation-threshold laser powers (Fig. 1c) that defines the geometry (for each Y row) of the printed object. Repeating this translation for each Y row in every Z plane, the required laser power at every point within the printer’s workspace is computed before the volume print scan is initiated. Power correction factors (see below) are applied to compensate for variable beam speed, spherical aberrations in the objective lens, or other nonuniformities. During printing, ScanImage executes a volume scan (as is typically performed for volumetric two-photon calcium imaging) using the laser power sequence precomputed by PrintImage (Fig. 1c), thus creating the printed object (Fig. 1d).

2.3 Calibration

To achieve maximum precision, calibration of imaging and printing parameters is necessary. We accomplish this by calibrating ScanImage’s optical workspace size parameters, using two methods: (1) producing fluorescent objects of known dimensions and imaging them with the rDLW printer, and (2) printing objects with the rDLW printer and measuring them on a calibrated device.

To create objects of precisely known dimensions, we used a commercial DLW printer to print rulers with IP-Dip photoresist (Fig. 2a; see Methods), and confirmed the dimensions of the rulers with SEM micrographs (the 10- μm ruler ticks measured 9.93 μm with a SEM two-pixel error $\pm 0.25 \mu\text{m}$). We imaged these rulers with our rDLW printer and adjusted ScanImage’s optical scaling parameters accordingly. We note that fluorescent rulers may be created without a calibrated DLW system [Khan and Brumberg, 2014].

To calibrate the X-Y plane, we printed calibration cubes (Fig. 2b) and a calibration ruler (Fig. 2c) with the rDLW printer, measured with SEM micrographs the discrepancy between desired and actual object dimensions, and adjusted ScanImage’s workspace size parameters to null the difference. Calibrating the Z print scale required printing a vertical calibration ruler (Fig. 2d) with regularly spaced Z planes that could be precisely measured using an optical surface profiler.

As the resonant scanner sweeps the laser’s focal point back and forth across the X axis of the printer’s workspace, the beam moves through the photoresist with sinusoidally varying velocity (Fig. 3a). If we define the centre of the sweep as $t = 0$, the oscillation frequency as F_r , and the maximum beam excursion as ξ , the focal point’s position x at time t is given by $x = \xi \sin(2\pi t F_r)$ (Fig. 3b, blue line). Beam velocity, $\delta x / \delta t$, rapidly approaches zero at the sweep extremes, so ScanImage restricts the usable portion of the raster scan to a central fraction, D , of the scan line, resulting in a printing workspace of width $2\xi D$. From the equation above, one sweep from $-\xi$ to ξ will take time $t = 1/(2F_r)$, so the beam will traverse the subsection spanning D in $t = 2 \arcsin(D)/(2\pi F_r)$. If laser power (controlled by the Pockels cell) has a modulation frequency of F_p , then power can be updated every $1/F_p$ seconds; this update rate enables $r_x = 2F_p \arcsin(D)/(2\pi F_r)$ potential changes in laser power level (i.e., printing voxels) during a single X-axis scan. In our instantiation, the resonant scanner

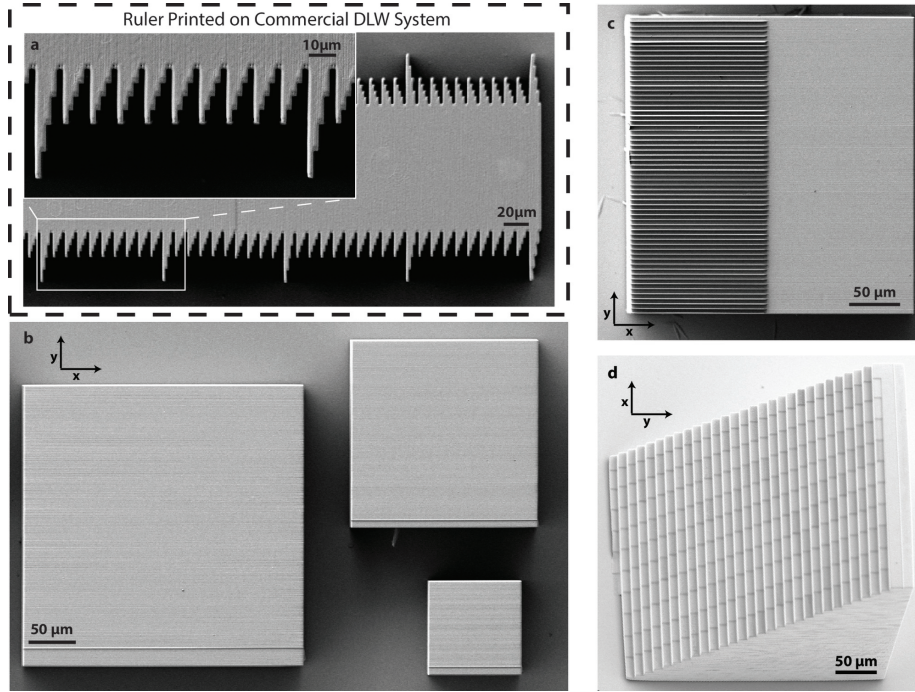


Figure 2: Rulers for calibrating the rDLW system. (a) Ruler for measuring X- and Y-workspace dimensions. (b) Cubes used to calibrate object size and uniformity of power delivery. The cubes shown have widths 300, 200, and 100 μm . The printing parameters were $2.2\times$ (i.e., $302 \times 302 \mu\text{m}$ FOV), $3.3\times$ and $6.6\times$ magnification (zoom), respectively. Each X-Y plane was built with 152×1024 voxels, and the vertical spacing between the planes was $0.5 \mu\text{m}$ for all three cubes. (c) Ruler for Y-axis calibration. The printing parameters are the same as for the 300- μm cube in (b). The horizontal line spacing on the ruler is $5 \mu\text{m}$. (d) Vertical ruler for Z-axis calibration. Each row along the X axis contains 11 steps with $1\text{-}\mu\text{m}$ height difference. Adjacent steps along the Y axis have $10\text{-}\mu\text{m}$ height difference. The total height of the ruler is $300 \mu\text{m}$. The printing parameters were the same as for the 300- μm cube in (b).

frequency ($F_r \approx 8$ kHz), the Pockels cell update rate ($F_p \approx 3.33$ MHz), and ScanImage’s workspace restriction ($D = 0.9$), result in a maximum of 152 print voxels along the X axis.

Resonant-scanner-based control results in higher resolution near the edges of its sweep than in the centre, but allows higher resolution as workspace size decreases. For example, on our rDLW system, printing at $1.3\times$ zoom yields a $512 \times 512\text{-}\mu\text{m}$ X-Y workspace. On the X axis, voxels are spaced on average every V/r_x for a workspace of span V , so at this zoom our rDLW printer is expected to have a $3.4\text{-}\mu\text{m}$ mean voxel size along the X axis. At $2.6\times$ zoom, the mean voxel size along X is expected to be $1.7\ \mu\text{m}$ over the $256 \times 256\text{-}\mu\text{m}$ workspace.

The use of a resonant scanner leads to significant variation about this mean, since laser power can be changed only at locations specified by the position function ($\xi \sin(2\pi t F_r)$; Fig. 3b, black ticks) at a frequency equal to the laser power modulation rate, F_p . Thus, actual voxel size should be nonuniform across the X axis, with smaller voxels at the edges of the workspace than near the center, proportional to $\cos(\arcsin x)$ for $x \in [-D\xi \dots D\xi]$ scaled and centred over V . As zoom level reduces workspace size V , expected voxel sizes over the X axis decrease linearly until they become limited by optics or photon wavelength (see Section 2.6).

2.4 Varying the laser power to ensure uniform printing

Given sinusoidally varying scan velocity (Fig. 3a) and constant laser power at the focal point, the photoresist will experience different light exposure conditions as the beam accelerates from the start of a raster line until it reaches peak velocity at the centre of the sweep and then decelerates as it approaches the end of a line. Under these conditions, the photoresist will not polymerise evenly, and may vaporise or boil in overexposed regions. Thus the baseline power of the polymerising laser must be corrected by a factor of $\cos(t) = \cos(\arcsin x)$ —proportional to the focal point’s speed—to maintain constant exposure.

Another source of variability in the laser energy available for polymerisation is attenuation of the beam due to inhomogenities in laser intensity over the workspace. This may be due to vignetting, which attenuates laser power toward the edges of the workspace, or to other effects such as those resulting from imperfect alignment of optical components. Falloff due to vignetting is complex, depending on the angles at which the laser enters and exits each lens in the system, relative alignments of all optical components, the shape of the laser beam, partial occlusions throughout the optical path, and possibly attenuation of the laser beam (although this should be minimal in its near field). Furthermore, some of these factors may change frequently in a developing multipurpose tool such as a two-photon microscope in a research setting.

Due to the difficulty of modeling these factors precisely, we use a simple adaptive approach to compensate for nonuniform optical fields. Given a model $M = f : x, y \rightarrow \text{falloff}$, power may be boosted by $1/M$ to compensate. The liquid photoresist used in these assays (IP-Dip) fluoresces when exposed to 390-nm light (i.e., two near-simultaneous 780-nm photons), and its refractive

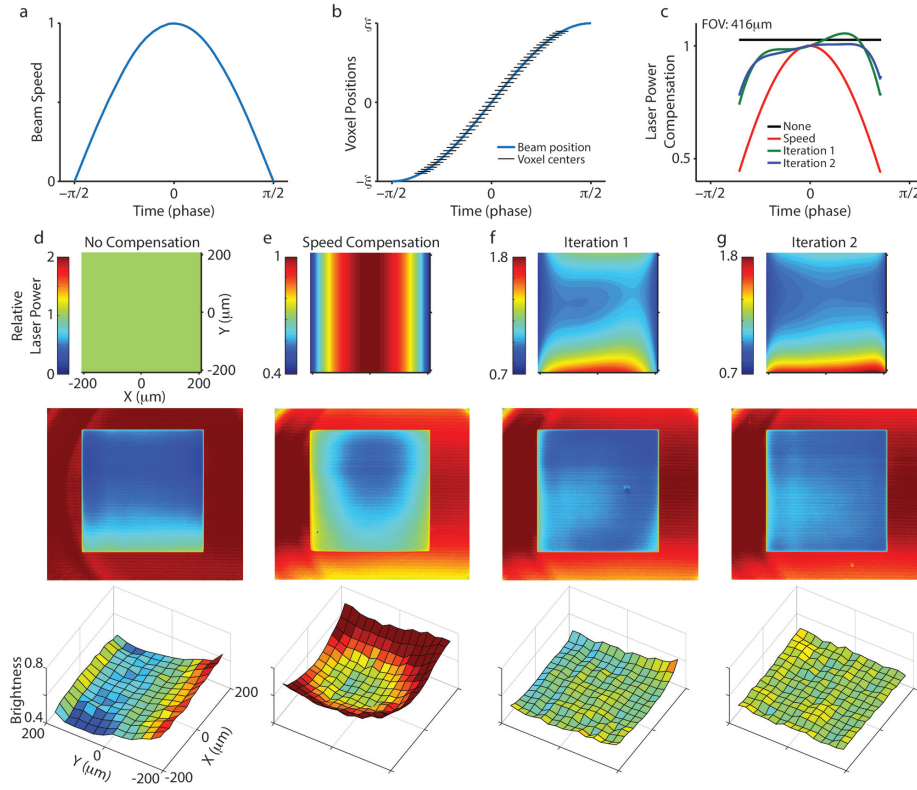


Figure 3: Sinusoidal laser velocity over the X axis results in nonuniform voxel size. Both that and optical nonuniformities such as vignetting require corrective laser power compensation. (a) Laser focal point velocity as the resonant scanner sweeps across the X axis. (b) Laser focus position varies sinusoidally with time (blue line). The active scanning region is restricted to a portion D of the sweep, with X-axis voxel positions shown as black horizontal dashes. For clarity, we show where voxels would be defined for an 8-kHz resonant scanner with a 1-MHz control system, which yields only 45 voxels. In order to maintain uniform energy deposition across the workspace, laser power is modulated by two factors: it is scaled along the X axis by the focal point's speed $\cos(t)$, and along the X-Y plane by a learned model of the inverse of optical darkening due to polymerisation. (c) Cross-section of the power compensation along X, in which $y = 0$, $x \in [-208, 208] \mu\text{m}$ ($1.6\times$ zoom on our rDLW system). (d-g) $400 \times 400 \times 100\text{-}\mu\text{m}$ bricks used to measure and calibrate energy deposition. The upper image shows the print power mask over the $208 \times 208\text{-}\mu\text{m}$ workspace; the middle image shows an actual printed object (normalised using a baseline fluorescence image); and the bottom image shows brightness data gathered by sweeping the object over the lens so that the same set of pixels in the imaging system may be used for each measurement in order to bypass optical nonuniformities therein. Shown: (d) constant power (note that (1) at this zoom optical vignetting comes close to compensating for X-axis nonuniformity due to varying beam speed; and (2) this image was printed at lower nominal power than the others in order to avoid boiling; for the other images, the speed compensation appropriately reduces power); (e) only (X-sinusoidal) speed power compensation; (f-g) two iterations of adaptive power compensation over the visual field (see text). The images and data were obtained with ScanImage on our rDLW system.

index and transparency are functions of the degree of polymerisation. Thus M may be approximated by measuring the reduction in fluorescence of polymerised photoresist over a uniform printed object (Methods). From these data we fit a curve such that falloff at any point may be interpolated (in Fig. 3 we use fourth-order polynomials in X and Y , although other functions may also be suitable). Due to the nonlinear relationships between applied laser power and degree of polymerisation [Mueller et al., 2014, Sun et al., 2003] and between degree of polymerisation and reduced fluorescence of the polymerised photoresist, this will not yield a perfect compensation model in one step, so the process may be iterated until sufficiently uniform energy deposition is achieved (Fig. 3f–g).

We assayed the uniformity of energy deposition across the workspace by printing $400 \times 400 \times 100\text{-}\mu\text{m}$ solid bricks and measuring the fluorescence variation across the printed objects (Fig. 3d–g) (see Methods). Simple beam speed power compensation—i.e., reducing power at the extrema of the X axis where the beam moves more slowly—was effective for producing even power deposition over small objects, but resulted in nonuniformities at $\lesssim 2.5\times$ zoom: the extreme edges of the X axis fluoresced more brightly than at the centre, indicating a lower degree of polymerisation. A compensation function fitted to the measured fluorescence variation increased the power at both the X and Y extrema, compensating for vignetting and other optical irregularities and resulting in nearly uniform polymerisation.

These two forms of power compensation—for focal-point speed and for optical inhomogenities—are important for uniform printing, but beyond that they demonstrate the ease with which polymerisation may be arbitrarily controlled on a per-voxel basis throughout printed objects, potentially allowing for easy development of techniques that take advantage of nonuniform polymerisation.

2.5 Accuracy

We estimated the accuracy of our rDLW system by printing simple geometric shapes (Fig. 2b–d) and comparing the final object dimensions with those of the original print model (measured with SEM micrographs for X and Y , and the surface profiler for Z). We found that print errors were not identical across the three dimensions, but instead varied by the print axis. Given that the laser focal position in 3D space is controlled by three distinct mechanisms (X axis: resonant scanning mirror; Y axis: galvanometer mirror; Z axis: piezo objective scanner), and that size is calibrated independently for each dimension, this is expected. For $300 \times 300\text{-}\mu\text{m}$ cubes printed at $2.2\times$ zoom, we found the errors in the size of the cube to be $-5.6 \pm 1.2 \mu\text{m}$ ($-1.9 \pm 0.4\%$) on the X axis and $6.5 \pm 1.0 \mu\text{m}$ ($2.2 \pm 0.33\%$) on the Y axis ($\pm x$ indicates SEM pixel size $x/2$). Z -axis accuracy was measured using the staircase ruler shown in Fig. 2d. Since our printing process leads to small variations (a few microns) in the starting height of the print, we measured Z accuracy at each step of the staircase (we leave more accurate automatic detection of substrate height for future work). The steps had a nominal height of $10 \mu\text{m}$, and an actual mean height of $10.0316 \mu\text{m}$ —an error of $\sim 0.32\%$, well within the surface profiler’s claimed accuracy of

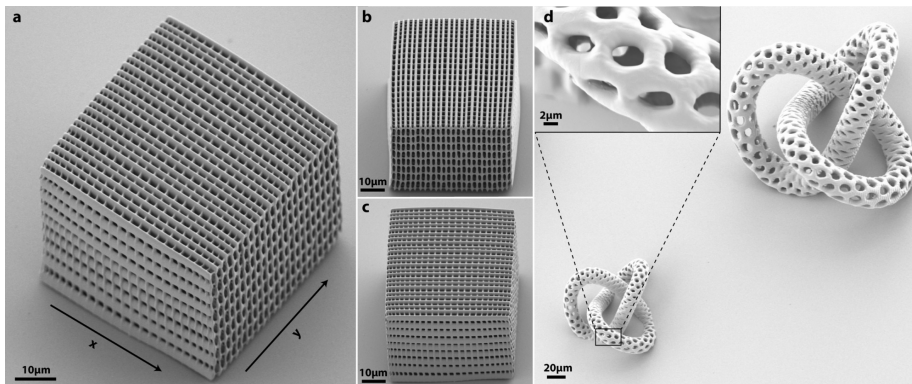


Figure 4: Complex geometric objects printed with our rDLW printer. (a-c) Woodpile structure with design dimensions $60 \times 60 \times 60 \mu\text{m}$. Along the X axis, bar thickness was 2 voxels ($0.8 \mu\text{m}$) and bar spacing 4 voxels ($1.6 \mu\text{m}$). Bar thickness and spacing on the Y axis were 13 and 26 voxels respectively in order to be the same size as the X-axis beams, and on the Z axis bars are 1 voxel thick with $6\text{-}\mu\text{m}$ spacing. The focal plane resolution was 152×1024 voxels, and the focal plane (Z) spacing was $0.2 \mu\text{m}$. (d) A torus knot design printed at $100 \times 100 \times 150 \mu\text{m}$ (top right) and $50 \times 50 \times 75 \mu\text{m}$ (bottom left). The inset shows details within the circumscribed region of the bottom left structure. Both knots were printed with focal plane resolution 152×512 voxels and focal plane spacing $0.2 \mu\text{m}$.

$< 0.75\%$.

All measurements were made following immersion of the printed objects in solvent to remove excess/unpolymerised resist (see Methods), and thus our estimates from SEM micrographs include some degree of post-processing-related object shrinkage. Achieving maximum printing accuracy—with this or any other DLW system—requires careful calibration, high-precision components, and control of post-processing deformation. Disentangling the contribution of each to our accuracy estimates is beyond the scope of this work.

2.6 Resolution

The minimum feature resolution of a two-photon polymerisation process is a nonlinear function of the precision of laser focal point control, laser power, and the chemical kinetics of the photoresist [LaFratta et al., 2007]. This complexity makes it challenging to predict the effective printing resolution of any DLW system, and thus each hardware configuration and photoresist combination must be verified experimentally.

One constraint on minimum feature size is the size of the laser’s focal point, as photon density is sufficiently high to initiate the polymerising reaction throughout this region. The laser focal point radial (i.e., along the X- and Y-axes) and axial (along the Z-axis) dimensions are functions of the laser’s wavelength, λ , and the numerical aperture, NA, of the objective lens. Assuming

an ideal (i.e., Gaussian) beam profile, the full-width half-maximum size of the point spread function is $\lambda/(2 \cdot \text{NA})$ (radial) and $\lambda/(2 \cdot \text{NA}^2)$ (axial) [Urey, 2004]. With our operating wavelength (780) nm and objective NA (0.8), the theoretical focal point dimensions are 488 and 609 nm, respectively. Other factors affect the effective size of the focal point—for example, if the laser beam incompletely fills the back of the objective, the effective NA will be lower, whereas changing the laser’s power will control the portion of the point spread function that crosses the polymerisation threshold [Kawata et al., 2001].

We treat the location of the centre of the focal point as the voxel location, since the degree to which it can be controlled defines another constraint on feature size. While the Y and Z positioning of the focal point are addressable with sub-micron accuracy via analogue control of the galvanometer mirror and the objective-lens scanner, respectively, the continuous sinusoidal motion of the resonant scanline along the X axis precludes direct control of position. Instead, X-axis voxel positions and sizes are defined by the rate at which the laser beam power can be modulated across the polymerisation threshold. Given the Pockels cell update frequency and the resonant scanner sweep rate, we estimate the X-axis resolution to be $\sim 2.5\text{--}5.6 \mu\text{m}$ (at the edge and centre of the resonant sweep, respectively) at $1\times$ zoom, with minimum feature size decreasing linearly with increasing magnification—for example, the $300\text{-}\mu\text{m}$ scale used for the resolution tests in Fig. 5 should have X voxel widths of $\sim 1.1\text{--}2.5 \mu\text{m}$ (edge and centre, respectively). In the following discussion we report only worst-case resolution—that at the centre of the X sweep.

Given these theoretical estimates of printer performance, we quantified real performance by printing objects with thin single-voxel features (Fig. 5a,b) and measuring feature dimensions using SEM micrographs. During polymerisation, the forming polymer tends to shrink due to both the emerging binding forces and polymerisation quenching from molecules present in the liquid solution. These effects are reduced when the forming polymer is attached to a solid object (e.g., a previously polymerised structure). We report the feature size as it is measured in features attached to a larger solid structure, but we also note the sizes of isolated features. We printed structures that consisted of channels containing single-voxel bridges, at $2.2\times$ zoom (an FOV of $302 \times 302 \mu\text{m}$). Because single-X-voxel bridges often broke during postprocessing, we also report 2-X-voxel-wide bridges. We estimated resolution by measuring the size of the bridges where they are attached to the supporting walls, and also estimated minimum size of suspended features—giving an idea of possible shrinkage—by measuring the bridges at their centre. Results are shown in Table 1.

The reported resolutions can be used to build complex thin-feature structures, such as the $60\text{-}\mu\text{m}$ woodpile shown in Fig. 4a–c and the hollow torus knot structure in Fig. 4d. Though these minimum feature sizes will be sufficient for some applications, further improvement is possible. As the X-axis voxel resolution is in part defined by the rate of laser power modulation, upgrading the Pockels cell and/or control hardware may produce a substantial reduction in feature size across the whole X axis. Improvement in all axes could be achieved by reducing the focal point size (e.g., by increasing the objective lens aperture,

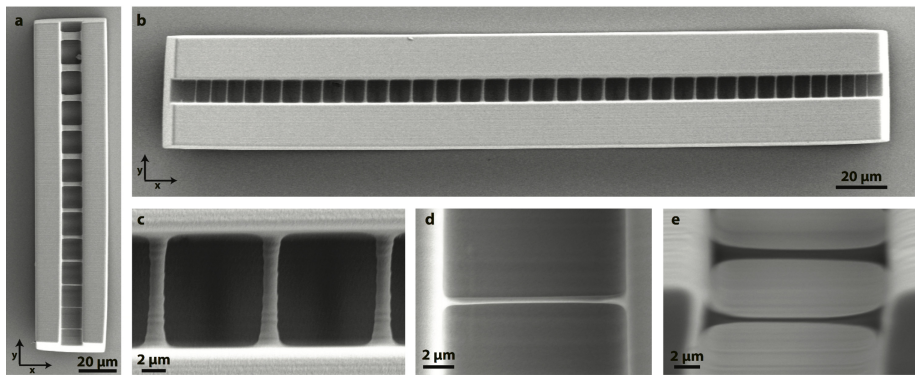


Figure 5: Objects with one- and two-voxel features printed on our rDLW system. (a) Object used to estimate minimum voxel size on the Y and Z axes. All bridges have single-voxel height (Z), and increasing width on the Y axis. The bottom bridge has one-voxel width; thus, it gives an idea of the thinnest suspended structure that can be achieved with the used parameters and photoresist. The object was printed with $2.2\times$ magnification for a $302\times 302\ \mu\text{m}$ field of view. The resolution of each focal plane is 152×1024 voxels, and the vertical distance between Z planes is $0.5\ \mu\text{m}$. (b) Object used to estimate the voxel size on the X axis. The printing parameters are the same as in (a). The bridges were designed to be two voxels wide on the X axis, so their size follows a sinusoidal distribution due to the cosinusoidal speed profile of the laser beam. (c) Top view of the central bridge of (b), which represents the largest value in the workspace of double-voxel X resolution at this zoom level. (d) Top view of the lowest bridge of (a). (e) View of the lowest bridge of (a) at 60° from the top view.

	Voxel dimension (μm)	Attached (μm)	Isolated (μm)
X	2.5/1.1	1.09 ± 0.14	0.3 ± 0.14
2X	5.0/2.2	2.73 ± 0.06	1.26 ± 0.06
Y	0.3	1.25 ± 0.03	0.35 ± 0.03
Z	0.5	2.10 ± 0.05	0.45 ± 0.05

Table 1: Printing resolution estimates. Resolution was estimated from SEM micrographs of the single- and double-voxel bridges in the objects shown in Fig. 5. Measurements of attached features were made proximal to the wall of the support structure; isolated-feature sizes were measured at the bridge centres. “Voxel dimension” is defined by the cell sizes used for voxelisation. We list theoretical voxel dimension for the X axis as two numbers: at the centre and edges of the resonant scanner’s sweep, respectively. We report measurements of X feature size at the centre of the resonant sweep—the region of the workspace in which we expect the largest minimum feature sizes. Discrepancies are expected due to the nonzero size and anisotropic shape of the focal point, postprocessing deformation, and a possible difference between rise and fall response times of our Pockels system.

flattening the beam profile, or reducing power [Kawata et al., 2001]), or using photoresists with higher polymerisation thresholds or reduced spatial expansion factors.

2.7 Speed

A key aim for our rDLW design was to increase fabrication speed through the introduction of a resonant scanner. As a first approximation, fabrication time is governed by two parameters: the speed with which the beam moves through the resist and the linear distance that the beam must traverse [Malinauskas et al., 2013]. DLW systems typically use some combination of stage-based (i.e., using motorised stages to move the printed object relative to a stationary laser focus) and mirror-based (i.e., using mirrors to move the laser focus relative to a objective’s stationary object) methods for polymerising the desired location. Each has its advantages, making direct comparisons challenging, but mirror-based scanning is capable of realising significantly higher scanning speeds while maintaining micro- and nanoscale feature sizes (Table 2).

Many DLW systems realise significant time savings by optimising the laser path such that travel distance is minimised. For printed objects with small fill ratios, this strategy can produce substantial improvements in fabrication speed. Other strategies, such as the core-and-shell printing process [Thiel et al., 2016], can reduce fabrication time for objects with low surface-area/volume ratios. Our approach achieves uniform fabrication times across fill ratios by using a resonant scanner to sweep the beam over every point in the printing workspace (Fig. 1b), maximising travel distance but at a higher mean speed than in many previously described systems (Table 2).

Positioning Mechanism	Scanning Speed (mm/s)	Nominal Feature Size (μm)	Reference
Stepper motor stage	10	1	[Kumi et al., 2010]
Piezo stage	0.03–0.09	0.28–1.5	[Straub and Gu, 2002]
	0.06	0.065	[Haske et al., 2007]
	10–30	1.5	[Ovsianikov et al., 2011]
Galvo-galvo mirror	0.005–0.2	0.085–1.5	[Thiel et al., 2010]
	0.01	1.3	[Maruo and Ikuta, 2000]
	7	0.78–1	[Farsari et al., 2006]
	0.4–200	0.2–1.2	[Obata et al., 2013]
	21–103	0.086–0.43	[Gottmann, 2009]
	400	1–10	[Skylar-Scott et al., 2016]
Rotating polygon-galvo mirror	7200	1	[Rensch et al., 1989]
Resonant-galvo mirror	3300–8200	1–4	Present work

Table 2: Representative DLW laser scanning speeds and nominal minimum feature sizes reported in recent literature. “Present work” gives scan speed with the printer configured as described for most of the examples in this paper ($1.6\times$ zoom yielding a $416 \times 416\text{-}\mu\text{m}$ workspace, and printing during only the left-to-right sweep of the resonant scanner) and the maximum speed that we’ve used (bidirectional printing at $1.3\times$ zoom). Minimum feature size and scan speed covary as described in the text.

In a resonant-scanner-based system with a resonant frequency of F_r and useable workspace dimensions of $2\xi D$ along the scanning dimension, the average beam speed is $2\xi DF_r$. For example, at $1.6\times$ zoom, our system’s useable workspace along the X axis is approximately $412\ \mu\text{m}$, resulting in an effective mean beam speed of $3.3\ \text{m/s}$. Note that this estimate assumes printing only in one direction of the laser scan (Fig. 1b); bi-directional printing effectively doubles beam speed, although any misalignment of the two scan directions leads to inferior results. Note also that decreasing magnification will increase the distance that the beam travels while commensurately increasing beam speed, leaving print time unchanged (provided that the laser can supply sufficient power to polymerise resist at the higher speed).

For our rDLW system, we can estimate fabrication time for an object from the linear printing distance (i.e., length of a scan line $2\xi D$ times the number of scan lines per layer S_y times the number of layers S_z) times the mean beam speed. For the large block in Fig. 2b, this results in an estimated fabrication

time of ~ 19 s, which comports well with our actual print time of ~ 25 s. DLW systems vary widely and there are no established benchmarks, making general comparisons of writing speed and printing time difficult [LaFratta et al., 2007, Sun and Kawata, 2004]. Galvanometer-based two-photon microscopes are typically an order of magnitude slower than resonant-scan microscopes. For example, at 512×512 pixels, resonant-scan microscopes typically achieve 30-Hz frame rates while typical galvo-based systems achieve ~ 1 –2-Hz frame rates at the same scan angle and resolution [Jonkman and Brown, 2015]. A pure galvanometer beam control system designed for calcium imaging might see a beam speed of 200 mm/s [Obata et al., 2013]. If such a system were used to write the simple block in Fig. 2b, fabrication would take about 3.8 minutes.

We emphasise that these calculations are for an object with a fill ratio of 1 (i.e., 100% of the total object volume is polymerised), so these estimates represents a worst-case fabrication time for an object of this size. Objects with smaller fill fractions—as would be likely for most objects of interest—would see reduced fabrication times on galvanometer- or stage-based systems that optimise beam path to reduce total travel distance. As with estimates of accuracy and resolution, our estimates of printing speed are highly dependent on our choice of optical components, printing parameters, and photoresist. Significant improvements or diminishments in all assayed metrics can be realised with a different choice of hardware, laser power, or row/layer density.

3 Discussion and Conclusion

We reported on rDLW: a 3D printer based on a standard two-photon microscope with a resonant raster scanner and our custom PrintImage control application. The rDLW system provides several key features including full access to fabrication parameters, high printing speeds, and ease of extensibility. Building on the widely-used open-source ScanImage microscopy package, this work provides a platform for future modifications and customisations.

Because our rDLW printer exposes all process parameters, and indeed all control software, to the user, our system is easily adaptable to experiments with novel fabrication techniques that take advantage of the unique feature of voxel-by-voxel modulation of laser power. This fine-grained power control proved useful in compensating for nonuniform optical effects such as vignetting, and could further be used to take advantage of intermediate states of polymerisation and the material properties that so arise (i.e., refractive index, rigidity, or fluorescence) [Gissibl et al., 2016b]. In addition, laser power is nonlinearly correlated with minimum feature resolution [Kawata et al., 2001], so per-voxel power modulation could provide additional control of the sizes of different single-voxel features in a single print process.

The use of a tunable femtosecond laser adds significant cost to our system, and could be replaced by fixed-wavelength fibre-based femtosecond sources. However, since tunable femtosecond lasers are common components of two-photon microscopes, we suggest that this more flexible laser may open up new

material choices for polymerisation at a range of wavelengths. We have demonstrated the capabilities of the system using IP-Dip, a proprietary refraction-index-matched photoresist designed for high-resolution two-photon polymerisation. However, the wide tunable range of modern two-photon laser sources (for our laser, 700–1050 nm), or the ease with which another laser can be added to the beam path, makes possible printing with commercial or custom resists having significantly different absorption spectrum peaks. This capability would simplify fabricating compound structures composed of multiple photoresists, each with different mechanical or optical properties [Zeng et al., 2015].

A limitation of existing DLW techniques—which not infrequently influences printed object design—is the need to add structural supports under suspended features, lest gravity and movement of the photoresist during printing displace the incomplete features before they are anchored to the body of the object being printed. An unexpected benefit of the rDLW system is that the high speed of printing allows, to some degree, the printing of unsupported, suspended features in viscous liquid photoresists (like IP-dip). In addition to streamlining object design, the ability to print without the need of support structure potentially enables the fabrication of previously unrealisable objects.

Though the maximum print size of the described rDLW system ($\sim 400 \times 400 \times 350 \mu\text{m}$) is suitable for many micro-scale applications, there are use cases (e.g., tissue culture scaffolding) that require larger object sizes while maintaining micron resolution. Several photoresists, including IP-Dip, Ormocer, and SU-8, allow newly polymerised material to bond directly onto previously polymerised material without mechanical defect. This allows an object to be built by stitching together several overlapping sections, each of which we refer to as a *metavoxel*. Additionally, whereas for a single metavoxel the zoom setting controls both X-axis resolution and maximum object size, stitching allows decoupling of these two parameters by printing a single piece as multiple smaller overlapping pieces at higher magnification. When stitching multiple metavoxels together, a stage with absolute linear accuracy on the order of the desired resolution is required. While a discussion of stitching is outside the scope of this paper, we note that, as of this writing, PrintImage allows stitching using either the microscopy stage or a commercial hexapod system, thus allowing fast printing of arbitrarily large objects, and it can easily be extended to use other hardware.

While resonant scanners have been previously used in 2D laser printing [Schermer and Dowd, 1990, Takeshi and Kaoru, 1995], a more common approach for raster-scan printing uses a multi-sided mirror rotating at constant speed to sweep the across the workspace [Takizawa and Kataoka, 1997]. Replacing the resonant scanner in our rDLW printer with such a raster-scan mirror would triple print speed by eliminating the flyback and near-zero-speed portions of the beam path. It would allow nearly linear beam speed, providing uniform voxel size and obviating sinusoidal power compensation. Though this would remove the resonant rDLW’s capacity to increase print resolution without a concomitant reduction in printing speed (i.e., zoom printing), a similar effect may be achievable by incorporating a zoom lens. Conversely, a change in

mirror rotation speed would allow changes in X-axis resolution without affecting workspace size.

4 Materials and Methods

4.1 Programming and analysis

All programming, modeling and analysis was done in MATLAB (The Mathworks, Framingham, MA) running under Windows 10 on a desktop computer with an Intel i7 processor and 16 GB of RAM. The PrintImage software is available at <https://github.com/gardner-lab/printimage>. Its documentation lists its software dependencies.

4.2 Design of calibration objects and print models

All custom benchmarking and example objects described here were created with Solidworks2016 (Dassault Systmes, Concord, MA) and exported using the native STL converter. Calibration objects not printed on our rDLW system (see Figure 2a) were printed using a Nanoscribe Photonic Professional GT (Nanoscribe GmbH, Stutensee, Germany). STL files for the Darwin Bust (Fig. 1d) and Torus Knot (Fig. 4c) were obtained from the Museum of Applied Arts and Sciences in Sydney, Australia and Tadej Skofic, respectively.

4.3 Photoresists and Post-Processing

A key step in developing a DLW solution is identifying photoresists that are compatible with both the specifications of the printing process (e.g., two-photon polymerisation, laser wavelength and power output, printing speed, etc.) and the requirements of the application (e.g., hardness, adhesion, biocompatibility, optical clarity, etc.). Though multiple photoresist formulations have been described, the majority used for two-photon DLW consist of soluble organic monomers or oligomers (typically acrylate derivatives) that are cross-linked, and thus made insoluble, by free radicals or cations produce by the exposure of a photoinitiator or photoacid generator [Fourkas, 2015]. The use of a tunable laser in the described rDLW system offers the possibility of printing with a variety of commercially available (e.g., Ormocer, KMPR, SU-8, etc.), custom, or proprietary photoresists.

In an effort to ensure that our assays were representative of the limits of our rDLW system’s performance, all objects reported here for illustration or benchmark measurements were printed with a high-performance photoresist, IP-Dip (Nanoscribe GmbH, Stutensee, Germany). IP-Dip is a proprietary liquid photoresist that is refraction-index-matched to glass to minimise optical distortion and enable rapid, fine-resolution two-photon polymerisation. IP-Dip polymerises under 390-nm light (i.e., the two-photon effective wavelength of our 780-nm source), producing solid, semi-transparent acrylic objects that have

been used in biomedical, optical, and microfluidic applications. Following printing, residual un-polymerised resist was removed by submerging the substrate and printed element in a solvent, propylene glycol methyl ether acetate (PGMEA), for approximately 20 min. The prints were then rinsed in methoxy-nonafluorobutane to remove trace PGMEA residue.

4.4 Scanning Electron Microscopy

Measurements of printed objects were made using SEM micrographs. To enhance sample conductivity, the samples were sputter-coated with gold prior to imaging. The samples were placed 3 cm under the gold target and were coated for 1 min at 0.05 mbar and 20 mA. The samples were imaged at 6-mm working distance with the secondary electron sensor, 3-kV accelerating voltage and 30- μm aperture size.

4.5 Energy Deposition Analysis

When IP-Dip polymerises, its fluorescent intensity changes, allowing printed objects to be imaged by exposing them to the laser at a power that causes fluorescence but is below the polymerisation threshold. The imaged fluorescent intensity is inversely proportional to the degree of polymerisation.

The energy deposition profile was quantified by measuring the fluorescent intensity of printed cubes at a depth of 5 μm below their top surfaces. Images were made using the ScanImage software at $1\times$ zoom, and were analysed in MATLAB. As vignetting at the extreme corners of the workspace reduces the laser’s intensity beyond our ability to compensate during printing, we restricted our analysis to objects up to $400\times 400\ \mu\text{m}$ ($1.6\times$ zoom). To eliminate the effects of spatial nonuniformity (such as vignetting) in our imaging system, rather than photographing still images and measuring brightness values over the imaging plane, we instead moved the printed objects under the lens (at 200 $\mu\text{m}/\text{s}$ along the X axis) using our stitching stage and recorded over time (at 15.21 Hz) the brightness values over the 1-pixel-by-10- μm XY region of the printed cube at the centre of the camera’s reference frame at each X-axis step. This was repeated for 15 equally spaced lines covering the Y axis. In order to compensate for the non-vignetting-corrected imaging laser power, a control image of the field of view without any objects was captured, and intensity values of the images of each test object were divided by the control image’s intensity.

5 Author Contributions

TJG and JMT conceptualised the project and implemented the initial proof of concept. BWP wrote the software for controlling the print process and integrated it with existing ScanImage routines. TMO and JMT designed the microscope modifications to enable the new printing process. CM developed test print objects, created calibration protocols, made all SEM micrographs,

and performed quantitative testing. BWP, TMO, and CM jointly contributed to device and process refinement. TJG and TMO supervised the project. BWP, CM, and TMO drafted the manuscript with input from all other authors.

6 Acknowledgments

We wish to thank Alice White (Boston University) for use of her Nanoscribe Photonic Professional GT 3D printing system and her expertise with microfabrication processes; Jacob Franklin (Vidrio Technologies) for his assistance with ScanImage; Tadej Skofic for designing the Torus Knot shown in Fig. 4; and the Museum of Applied Arts and Sciences in Sydney, Australia for providing the bust of Darwin shown in Fig. 1. We also wish to thank Alberto Cruz-Martin, Todd Blute, Ian Davison, Jeff Gavornik, and L. Nathan Perkins for their helpful comments on earlier drafts of this manuscript. Furthermore, we are grateful for the packages on the MATLAB File Exchange from Alex A (Mesh voxelisation), Eric Johnson (STL File Reader), Pau Micó (stlTools), and Teck Por Lim (Significant Figures). This research was supported by NIH grants (U01NS090454 and R01NS089679) and a sponsored research agreement with GlaxoSmithKline.

References

- J. H. Atwater, P. Spinelli, E. Kosten, J. Parsons, C. Van Lare, J. Van De Groep, J. Garcia De Abajo, A. Polman, and H. A. Atwater. Microphotonic parabolic light directors fabricated by two-photon lithography. *Applied Physics Letters*, 99(15):39–42, 2011. ISSN 00036951. doi: 10.1063/1.3648115.
- Tiemo Buckmann, Nicolas Stenger, Muamer Kadic, Johannes Kaschke, Andreas Frlich, Tobias Kennerknecht, Christoph Eberl, Michael Thiel, and Martin Wegener. Tailored 3d mechanical metamaterials made by dip-in direct-laser-writing optical lithography. *Advanced Materials*, 24(20):2710–2714, 2012. ISSN 1521-4095. doi: 10.1002/adma.201200584.
- Brian H. Cumpston, Sundaravel P. Ananthavel, Stephen Barlow, Daniel L. Dyer, Jeffrey E. Ehrlich, Lael L. Erskine, Ahmed A. Heikal, Stephen M. Kuebler, I. Y. Sandy Lee, Dianne McCord-Maughon, Jinqi Qin, Harald Rockel, Mariacristina Rumi, Xiang-Li Wu, Seth R. Marder, and Joseph W. Perry. Two-photon polymerization initiators for three-dimensional optical data storage and microfabrication. *Nature*, 398(6722):51–54, 03 1999. doi: 10.1038/17989.
- M. Farsari and B. N. Chichkov. Materials processing: Two-photon fabrication. *Nature Photonics*, 3:450–452, August 2009. doi: 10.1038/nphoton.2009.131.
- Maria Farsari, George Filippidis, Kyriaki Sambani, Theodore S. Drakakis, and Costas Fotakis. Two-photon polymerization of an eosin y-sensitized acrylate composite. *Journal of Photochemistry and Photobiology A: Chemistry*, 181(1):

- 132–135, 2006. ISSN 10106030. doi: 10.1016/j.jphotochem.2005.11.025. URL <http://linkinghub.elsevier.com/retrieve/pii/S1010603005006015>.
- John Fourkas. Fundamentals of two-photon fabrication. In T. Baldacchini, editor, *Three-dimensional Microfabrication Using Two-photon Polymerization: Fundamentals, Technology, and Applications*, Micro and Nano Technologies Series. William Andrew Publishing, 2015. ISBN 9780323353212. URL https://books.google.com/books?id=e-_SsgEACAAJ.
- Rafael R. Gattass and Eric Mazur. Femtosecond laser micromachining in transparent materials. *Nature Photonics*, 2:219–225, 2008. doi: doi:10.1038/nphoton.2008.47. URL <http://www.nature.com/nphoton/journal/v2/n4/full/nphoton.2008.47.html>.
- Timo Gissibl, Simon Thiele, Alois Herkommer, and Harald Giessen. Submicrometre accurate free-form optics by three-dimensional printing on single-mode fibres. *Nature Communications*, 7:11763, 2016a. ISSN 2041-1723. doi: 10.1038/ncomms11763. URL <http://www.nature.com/doifinder/10.1038/ncomms11763>.
- Timo Gissibl, Simon Thiele, Alois Herkommer, and Harald Giessen. Two-photon direct laser writing of ultracompact multi-lens objectives. *Nature Photonics*, 10(8):554–560, 2016b. ISSN 1749-4885. doi: 10.1038/nphoton.2016.121. URL <http://www.nature.com/doifinder/10.1038/nphoton.2016.121>.
- Jens Gottmann. High speed and high precision fs-laser writing using a scanner with large numerical aperture. *Journal of Laser Micro/Nanoengineering*, 4(3):192–196, 2009. ISSN 18800688. doi: 10.2961/jlmn.2009.03.0009. URL <http://www.jlps.gr.jp/jlmn/upload/caa47af5bee5126d2b828f9a2fd74116.pdf>.
- W Haske, V.W. Chen, J.M. Hales, W Dong, S Barlow, S.R. Marder, and Joseph Perry. 65 nm feature sizes using visible wavelength 3-d multiphoton lithography. *Optics Express*, 15(6), 2007.
- James Jonkman and Claire M Brown. Any way you slice it a comparison of confocal microscopy techniques. *Journal of Biomolecular Techniques*, 26(2): 54–65, 2015. doi: 10.7171/jbt.15-2602-003. URL <https://www.ncbi.nlm.nih.gov/pmc/articles/PMC4365987/>.
- Elmina Kabouraki, Konstantina Terzaki, Vasileia Melissinaki, Maria Manousidaki, Maria Vamvakaki, and Maria Farsari. Direct fs Laser Writing of 3D Nanostructures. In *Direct fs Laser Writing of 3D nanostructures*, chapter 8, pages 3–30. 2015. ISBN 978-3-319-12216-8. doi: 10.1007/978-3-319-12217-5. URL <http://link.springer.com/10.1007/978-3-319-12217-5>.
- Satoshi Kawata, Hong-Bo Sun, Tomokazu Tanaka, and Kenji Takada. Finer features for functional microdevices. *Nature*, 412:697–698, August 2001. doi: doi:10.1038/35089130.

- Safraz Khan and Joshua C. Brumberg. An inexpensive fluorescent graticule. *Microscopy Today*, pages 26–27, Jan 2014. doi: 10.1017/S1551929513001326.
- George Kumi, Ciceron O. Yanez, Kevin D. Belfield, and John T. Fourkas. High-speed multiphoton absorption polymerization: fabrication of microfluidic channels with arbitrary cross-sections and high aspect ratios. 10(8): 1057, 2010. ISSN 1473-0197, 1473-0189. doi: 10.1039/b923377f. URL <http://xlink.rsc.org/?DOI=b923377f>.
- Christopher N. LaFratta, John T. Fourkas, Tommaso Baldacchini, and Richard A. Farrer. Multiphoton fabrication. *Angewandte Chemie International Edition*, 46(33):6238–6258, 2007. ISSN 1521-3773. doi: 10.1002/anie.200603995.
- Mangirdas Malinauskas, Albertas Zukauskas, Vytautas Purlys, Kastytis Belazaras, Andrej Momot, Domas Paipulas, Roaldas Gadonas, Algis Piskarskas, Holger Gilberts, Arunė Gaidukevičiūtė, Ioanna Sakellari, Maria Farsari, and Saulius Juodkazis. Femtosecond laser polymerization of hybrid/integrated micro-optical elements and their characterization. *Journal of Optics*, 12(12):124010, 2010. URL <http://stacks.iop.org/2040-8986/12/i=12/a=124010>.
- Mangirdas Malinauskas, Maria Farsari, Algis Piskarskas, and Saulius Juodkazis. Ultrafast laser nanostructuring of photopolymers: A decade of advances. *Physics Reports*, 533(1):1–31, 2013. ISSN 0370-1573. doi: <http://dx.doi.org/10.1016/j.physrep.2013.07.005>. URL <http://www.sciencedirect.com/science/article/pii/S0370157313002718>.
- Shoji Maruo and Koji Ikuta. Three-dimensional microfabrication by use of single-photon-absorbed polymerization. *Applied Physics Letters*, 76(19):2656–2658, 2000. ISSN 0003-6951, 1077-3118. doi: 10.1063/1.126742. URL <http://aip.scitation.org/doi/10.1063/1.126742>.
- Shoji Maruo, Osamu Nakamura, and Satoshi Kawata. Three-dimensional microfabrication with two-photon-absorbed photopolymerization. *Opt. Lett.*, 22(2):132–134, Jan 1997. doi: 10.1364/OL.22.000132. URL <http://ol.osa.org/abstract.cfm?URI=ol-22-2-132>.
- Jonathan B. Mueller, Joachim Fischer, Frederik Mayer, Muamer Kadic, and Martin Wegener. Polymerization kinetics in three-dimensional direct laser writing. *Advanced Materials*, pages 6566–6571, 2014. ISSN 09359648. doi: 10.1002/adma.201402366.
- Fabian Niesler and Yann Tanguy. 3d printers for the fabrication of micro-optical elements. *Optik & Photonik*, 11(4), 2016. doi: 10.1002/opph.201600028.
- Kotaro Obata, Ayman El-Tamer, Lothar Koch, Ulf Hinze, and Boris N Chichkov. High-aspect 3d two-photon polymerization structuring with

- widened objective working range (WOW-2pp). *Light: Science & Applications*, 2(12):e116, 2013. ISSN 2047-7538. doi: 10.1038/lisa.2013.72. URL <http://www.nature.com/doi/10.1038/lisa.2013.72>.
- Aleksandr Ovsianikov, Andrea Deiwick, Sandra Van Vlierberghe, Peter Dubruel, Lena Mller, Gerald Drger, and Boris Chichkov. Laser fabrication of three-dimensional CAD scaffolds from photosensitive gelatin for applications in tissue engineering. *Biomacromolecules*, 12(4):851–858, 2011. ISSN 1525-7797, 1526-4602. doi: 10.1021/bm1015305. URL <http://pubs.acs.org/doi/abs/10.1021/bm1015305>.
- TA Pologruto, BL Sabatini, and K. Svoboda. Scanimage: flexible software for operating laser scanning microscopes. *Biomed Eng Online*, 2003. doi: 10.1186/1475-925X-2-13. URL <https://www.ncbi.nlm.nih.gov/pubmed/12801419>.
- Clemens Rensch, Stefan Hell, Manfred v Schickfus, and Siegfried Hunklinger. Laser scanner for direct writing lithography. *Applied optics*, 28(17):3754–3758, 1989.
- Mack J. Schermer and Roger D. Dowd. Resonant scanner control system, 1990. URL <https://www.google.com/patents/US5121138>. U.S. Patent 5121138.
- M. A. Skylar-Scott, M.-C. Liu, Y. Wu, and M. F. Yanik. Multi-photon microfabrication of three-dimensional capillary-scale vascular networks. In *Society of Photo-Optical Instrumentation Engineers (SPIE) Conference Series*, volume 10115, February 2017. doi: 10.1117/12.2253520.
- Mark A. Skylar-Scott, Man-Chi Liu, Yuelong Wu, Atray Dixit, and Mehmet Fatih Yanik. Guided homing of cells in multi-photon microfabricated bioscaffolds. *Advanced Healthcare Materials*, 5(10):1233–1243, 2016. ISSN 2192–2659. doi: 10.1002/adhm.201600082.
- Martin Straub and Min Gu. Near-infrared photonic crystals with higher-order bandgaps generated by two-photon photopolymerization. *Optics Letters*, 27(20), 2002. doi: 10.1364/OL.27.001824. URL <https://www.osapublishing.org/ol/abstract.cfm?uri=ol-27-20-1824>.
- Hong-Bo Sun and Satoshi Kawata. Two-photon photopolymerization and 3d lithographic microfabrication. In *NMR 3D Analysis Photopolymerization*, pages 169–273. Springer Berlin Heidelberg, Berlin, Heidelberg, 2004. ISBN 978-3-540-40000-4. doi: 10.1007/b94405.
- Hong-Bo Sun, Kenji Takada, Moon-Soo Kim, Kwang-Sup Lee, and Satoshi Kawata. Scaling laws of voxels in two-photon photopolymerization nanofabrication. *Applied Physics Letters*, 83(6):1104–1106, 2003. doi: 10.1063/1.1599968.

- Takeshi and Kaoru. Scanning device with resonant light deflector, February 8 1995. URL <http://google.com/patents/EP0637885A1?cl=zh-cn>. EP Patent App. EP19,940,111,183.
- N. Takizawa and E. Kataoka. Laser beam printing device with mirror rotation speed controlled by origin sensor signal, October 14 1997. URL <https://www.google.com/patents/US5677724>. US Patent 5,677,724.
- M. Thiel, J. Fischer, G. von Freymann, and M. Wegener. Direct laser writing of three-dimensional submicron structures using a continuous-wave laser at 532 nm. *Applied Physics Letters*, 97(22):221102, 2010. ISSN 0003-6951, 1077-3118. doi: 10.1063/1.3521464. URL <http://aip.scitation.org/doi/10.1063/1.3521464>.
- Michael Thiel, Roman Reinhard Reiner, Fabian Niesler, and Yann Tanguy. Method for producing a three-dimensional structure, 2016. URL <https://www.google.com/patents/US20160114530>. U.S. Patent 20160114530.
- Hakan Urey. Spot size, depth-of-focus, and diffraction ring intensity formulas for truncated gaussian beams. *Appl. Opt.*, 43(3):620–625, Jan 2004. doi: 10.1364/AO.43.000620. URL <http://ao.osa.org/abstract.cfm?URI=ao-43-3-620>.
- Hao Zeng, Piotr Wasylczyk, Camilla Parmeggiani, Daniele Martella, Matteo Burrelli, and Diederik Sybolt Wiersma. Light-Fueled Microscopic Walkers. *Advanced Materials*, 27(26):3883–3887, 2015. ISSN 09359648. doi: 10.1002/adma.201501446. URL <http://www.pubmedcentral.nih.gov/articlerender.fcgi?artid=4660875>.